


Interference from interband harmonics generated by different crystal momentum channels

Shuang Wang, Si-Tong Liu, Xiao-Xin Huo, Yun-He Xing, and Jun Zhang*
Institute of Atomic and Molecular Physics, Jilin University, Changchun 130012, China

 (Received 12 June 2023; revised 21 September 2023; accepted 7 November 2023; published 18 December 2023)

We theoretically investigate the high-order harmonic generation (HHG) of zinc oxide (ZnO) induced by linearly polarized laser pulses. It is found that the harmonic spectrum exhibits fine subpeak structures, which is related to the interband polarization arising from electron-hole interactions. Further numerical analyses show that the subpeak structures originate from the interference between the interband harmonics, which are generated by different crystal momentum channels around the top of the valence band. Additionally, we extend our inquiry to solid HHG driven by a two-color laser field. Intriguingly, our findings indicate a notable suppression of harmonic subpeak structures in this context. To gain insight into the governing physical mechanisms, we illustrate the time-dependent population in the conduction band. Our analysis underscores a phenomenon of electron preacceleration before ionization. Consequently, the crystal momentum channels around the top of the valence band exhibit diminished contributions to HHG, leading to the effective suppression of harmonic subpeak structures. Our results may provide insights into the underlying mechanisms of solid HHG.

DOI: [10.1103/PhysRevA.108.063106](https://doi.org/10.1103/PhysRevA.108.063106)

I. INTRODUCTION

Over the preceding decades, extensive research efforts have been dedicated to the exploration of high-order harmonic generation (HHG) in atomic and molecular systems [1–6], a phenomenon often elucidated through the semiclassical three-step model [7]. Compared with the gas phase, the solids have distinct characteristics, including natural crystal orientation, high electron density, and periodic structure, which make the harmonic emission process of solid materials attract much attention [8–14]. The solid HHG originates from two main mechanisms, intra- and interband currents [15], i.e., the electrons are initially excited from the valence band (V-B) to the conduction band (C-B) driven by the intense laser field, and then the electrons or holes are accelerated under the laser field. Finally, the recombination of electrons with holes leads to the emission of harmonic photons. For solid systems, it has been proved that the HHG is sensitive to the waveform of the two-color laser field [16–19]. The two-color laser field contains many more control parameters than a monochromatic laser field, which can help to achieve the spectral modulations by controlling the laser parameters.

HHG in solids holds substantial implications across a diverse array of applications, such as reconstructing band structures [20–22], measuring the Berry curvature [23,24], and controlling ultrafast electron dynamics [16,25,26]. Lang *et al.* [27] theoretically revealed that the previously generated high harmonics can participate in the latter nonlinear dynamics, which led to the nonlinear gain and cutoff extension of harmonics. Recently, by resolving the oscillation phase of harmonics as a function of crystal, the HHG of MgO has been

successfully used to probe the light-induced modification of the band structure in experiments [28].

Interferences during the HHG processes have been investigated theoretically and experimentally [29–37]. The interference effect between intra- and interband currents in HHG of ZnO crystal has been demonstrated. It is found that the constructive and destructive interferences between intra- and interband currents cause the harmonic spectra to split into some fine subpeak structures [33]. Furthermore, quantum interference, manifested as an outcome of short and long electron trajectories, has been elucidated as a cause of spectral splitting in solid-state HHG under the influence of intense laser fields [34]. The interference between harmonics generated by different crystal momentum channels can also modulate the harmonic spectrum. For instance, the suppression of even-order harmonics has been attributed to destructive interference arising from a set of symmetrical crystal momentum channels [35,36].

Recent investigations have underscored the significance of comprehending crystal-momentum-resolved contributions in solid HHG [35–39]. Given the direct correlation between crystal momentum channels and the underlying crystal structure, it is expected that the solid HHG can be used to detect the physical properties of materials. This is accomplished by independently considering contributions from various initial crystal momenta [38]. Lü *et al.* [37] investigated the crystal-momentum-resolved intraband harmonics by using the preexcitation pulse. They found an abnormal dependence of intraband HHG yield on the laser intensity, which is due to the coherence of harmonics emitted from different electrons. Additionally, the electrons ionized far from the top of V-B have been demonstrated to be responsible for the multiple plateaus of HHG [39].

In this paper, we investigate the HHG of ZnO by solving the semiconductor Bloch equations (SBEs). By analyzing

*junzhang@jlu.edu.cn

the crystal-momentum-resolved interband harmonics, we find that the interference between harmonics of different crystal momentum channels induces the harmonic subpeak structures. When we use an appropriate two-color laser field, the harmonic subpeak structures are suppressed. Further analyses demonstrate that the preacceleration processes occur before the electrons are ionized by illustrating the time-dependent population in the C-B. This paper is organized as follows. In Sec. II, we mainly introduce the theoretical approach. In Sec. III, we present the numerical simulation results and discussions in detail. Conclusions are given in Sec. IV.

II. THEORETICAL METHODS

In this paper, we investigate the interaction of intense lasers with the two-band ZnO crystal by the solution of the one-dimensional semiconductor Bloch equations (SBEs) [12,15,35,40], which can be expressed by (unless specified, we use atomic units throughout)

$$\dot{n}_m = i \sum_{m \neq m'} \Omega_{mm'} \pi_{mm'} e^{iS_{mm'}} + \text{c.c.}, \quad (1)$$

$$\begin{aligned} \dot{\pi}_{mm'} = & -\frac{\pi_{mm'}}{T_2} + i\Omega_{mm'}^* (n_m - n_{m'}) e^{-iS_{mm'}} \\ & + i \sum_{m'' \notin \{m, m'\}} (\Omega_{m'm''} \pi_{mm''} e^{iS_{m'm''}} - \Omega_{mm''}^* \pi_{m'm''}^* e^{-iS_{mm''}}), \end{aligned} \quad (2)$$

where $n_m(\mathbf{K}, t)$ is the population of band m . $m = v$ stands for the V-B and $m = c$ stands for the C-B. Initially all electrons are in the V-B. According to the Bloch acceleration theorem [41], the initial crystal momentum \mathbf{k} can be transformed to a moving momentum frame by $\mathbf{K} = \mathbf{k} - \mathbf{A}(t)$, where $\mathbf{A}(t)$ is the vector potential of the electric field. As a result, the first Brillouin zone (BZ) is also shifted to $\overline{BZ} = BZ - \mathbf{A}(t)$. $\pi_{mm'}(\mathbf{K}, t)$ is the polarization strength between the V-B and C-B. $\Omega_{mm'}(\mathbf{K}, t) = \mathbf{E}(t) \cdot \mathbf{d}_{mm'}[\mathbf{K} + \mathbf{A}(t)]$ is the Rabi frequency. $\mathbf{d}_{mm'}[\mathbf{K} + \mathbf{A}(t)]$ is the crystal-momentum-dependent transition dipole moment. $S_{mm'}(\mathbf{K}, t) = \int_{-\infty}^t \varepsilon_{mm'}[\mathbf{K} + \mathbf{A}(t')] dt'$ is the classical action with band energy difference $\varepsilon_{mm'} = E_m - E_{m'}$. We set $T_2 = 2.75$ fs to depict the dephasing process between two bands in the solid HHG.

The intraband current $\mathbf{j}_{ra}(t)$ and interband current $\mathbf{j}_{er}(t)$ can be written as [18,38,39]

$$\mathbf{j}_{ra}(t) = \sum_m \int_{\overline{BZ}} \mathbf{v}_m[\mathbf{K} + \mathbf{A}(t)] n_m(\mathbf{K}, t) d\mathbf{K}, \quad (3)$$

$$\mathbf{j}_{er}(t) = \frac{d}{dt} \sum_{m \neq m'} \int_{\overline{BZ}} [\mathbf{d}_{mm'} \pi_{mm'}(\mathbf{K}, t) e^{iS_{mm'}} + \text{c.c.}] d\mathbf{K}, \quad (4)$$

where $\mathbf{v}_m(\mathbf{k}) = \nabla_{\mathbf{k}} E_m(\mathbf{k})$ and $E_m(\mathbf{k})$ are the band velocity and band dispersion, respectively.

The total harmonic spectrum is proportional to the absolute square of the Fourier transform of laser-induced current [15,35,40]

$$S_{\text{total}}(\omega) = \omega^2 \left| \int [\mathbf{j}_{ra}(t) + \mathbf{j}_{er}(t)] e^{-i\omega t} dt \right|^2. \quad (5)$$

The intraband and interband contributions to the harmonic spectrum can be written as

$$S_{ra}(\omega) = \omega^2 \left| \int \mathbf{j}_{ra}(t) e^{-i\omega t} dt \right|^2, \quad (6)$$

$$S_{er}(\omega) = \omega^2 \left| \int \mathbf{j}_{er}(t) e^{-i\omega t} dt \right|^2. \quad (7)$$

In our simulation, the laser field can be written as

$$E(t) = f(t)[E_0 \cos(\omega_0 t) + E_1 \cos(3\omega_0 t + \phi)], \quad (8)$$

where $f(t) = \exp[-2 \ln(2)t^2/\tau^2]$ is a Gaussian-type envelope with the full width at half maximum (FWHM) $\tau = 6$ o.c. (optical cycle). $E_0 = 0.0046$ a.u. is the amplitude of the fundamental field, and $\omega_0 = 0.021$ a.u. is the corresponding frequency of the laser field. In the following, $E_1 = 0$ for the one-color laser field. For the two-color laser field, the field ratio $E_1/E_0 = 0.4$ and the relative phase $\phi = \pi$.

III. RESULTS AND DISCUSSION

A. Harmonic subpeak structures caused by interference effect

Figure 1(a) depicts the HHG spectra induced by the one-color linearly polarized laser field, where the peak of the electric field is $E_0 = 0.0046$ a.u., and the laser frequency is $\omega_0 = 0.021$ a.u.. The FWHM is $\tau = 6$ o.c., and the total duration of the laser pulse is 25 o.c. in our simulations. From Fig. 1(a), one can see that the spectrum integrated over the first BZ (represented by the red solid line) exclusively exhibits odd-order harmonics due to the inversion symmetry about the Γ point [35]. We also find that the harmonic spectrum appears in some subpeak structures around the plateau region. These subpeak structures, akin to those observed in high harmonic generation from bulk sapphire in experimental studies [34], are interpreted as a manifestation of interference effects. Consequently, it is plausible to attribute the subpeak structures observed in Fig. 1(a) to interference effects. In particular, the electron has the highest excitation probability for the C-B at the Γ point (\mathbf{k}_0 channel), due to the minimum band gap. As a result, we further analyze the harmonic spectrum while considering only the \mathbf{k}_0 channel as indicated by the blue dotted-dashed line in Fig. 1(a), which exclusively exhibits odd-order harmonics without subpeak structure.

To elucidate the nature of these subpeak structures, Fig. 1(b) presents harmonic spectra in the vicinity of the 13th order. We can see that the intraband harmonic spectrum displays an ordinary structure, while the interband and total harmonic spectra display fine peaks. The interband harmonic yield (yellow dotted line) coincides exactly with the total harmonic yield (red solid line), which justifies that the subpeaks in Fig. 1(a) come from the interband harmonic contribution. Our results differ from the case that the intra- and interband interferences make the harmonic split into several subpeaks, as demonstrated in Ref. [33]. In Ref. [33], the intra- and interband harmonic intensities are comparable. Thus, their interferences will noticeably affect the total harmonic spectrum and create the subpeak structures. In Fig. 1(b), however, we can see that the interband harmonic intensity surpasses that of the intraband harmonic by two to three orders of magnitude, rendering the interference effect between intra- and interband

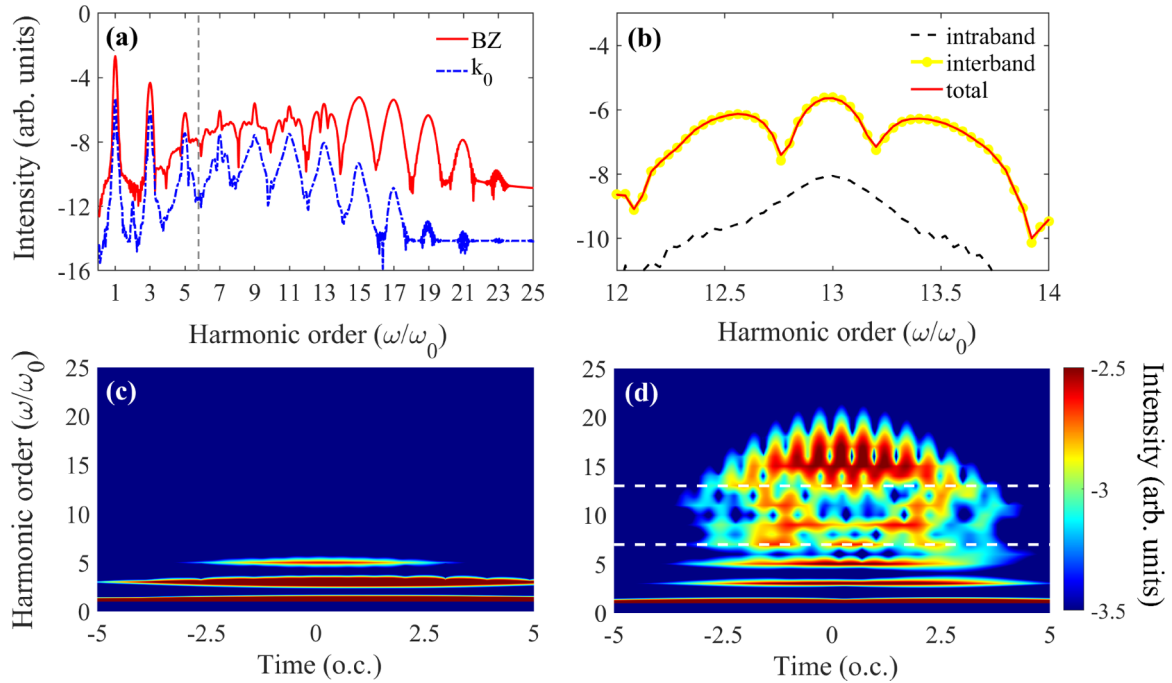


FIG. 1. (a) The total HHG spectra integrated over the first BZ (red solid line) and generated by the \mathbf{k}_0 channel (blue dotted-dashed line). The vertical gray dashed line represents the harmonic order corresponding to the minimum energy band gap ($\varepsilon_g = 3.3$ eV). (b) Harmonic spectra from intraband (black dashed line), interband (yellow dotted line), and total (red solid line) currents. (c) and (d) Time-frequency analysis of intraband and interband HHG, respectively. The white dashed lines in (d) represent the positions of the 7th and 13th order.

currents negligible. It is expected that a different mechanism of harmonic radiation may be responsible for these subpeak structures.

Figures 1(c) and 1(d) illustrate the time-frequency spectra corresponding to intra- and interband HHG, respectively. From Fig. 1(c), the time-frequency distribution of the intraband harmonic spectrum displays an ordinary structure. From Fig. 1(d), we can see that some unusual minima peaks show up from the 7th to the 13th order harmonic, which demonstrates that the interband harmonic contributes to the harmonic subpeak structures [see Fig. 1(a)]. Similar structures have been shown in the wavelet time-frequency spectrum of hydrogen molecular ions [32]. They found that these fine structures are due to the interference in cycles of the multiphoton radiation. Thus, the underlying mechanisms for these subpeak structures are still desired.

The SBEs in the Houston representation are uncoupled for different initial crystal momentum \mathbf{k} and can be independently solved for each \mathbf{k} [35]. Thus, we used 401 equally spaced \mathbf{k} points to sample the first BZ $[-\frac{\pi}{a}, \frac{\pi}{a}]$ for SBE simulations, where $a = 5.32$ is the lattice constant. In the following, we set \mathbf{k}_i ($i = -200, -199, \dots, 200$) as a specific crystal momentum channel of each \mathbf{k} point for the first BZ. The intra- and interband currents for each initial crystal momentum \mathbf{k} can be written as [18,38]

$$\mathbf{j}_{ra}^{\mathbf{k}}(t) = \sum_m \mathbf{v}_m[\mathbf{K} + \mathbf{A}(t)]n_m(\mathbf{K}, t), \quad (9)$$

$$\mathbf{j}_{er}^{\mathbf{k}}(t) = \frac{d}{dt} \sum_{m \neq m'} \mathbf{d}_{mm'} \pi_{mm'}(\mathbf{K}, t) e^{iS_{mm'}} + \text{c.c.} \quad (10)$$

According to the semiclassical acceleration theorem, the instantaneous crystal momentum \mathbf{K} of an electron is $\mathbf{k} - \mathbf{A}(t)$, with the initial crystal momentum \mathbf{k} and the vector potential $\mathbf{A}(t)$. Consequently, the initial crystal momentum has been transformed into a frame moving with the vector potential [12,15,35,40], i.e., $\mathbf{K} = \mathbf{k} - \mathbf{A}(t)$. This transformation also causes a shift of the first BZ to $\overline{BZ} = BZ - \mathbf{A}(t)$. The integration over the first BZ results in the total intra- and interband currents as illustrated in Eqs. (3) and (4), respectively.

To investigate the contributions to HHG from electrons with different initial crystal momenta, we depict the intra- and interband harmonic spectra as a function of the initial crystal momentum in Fig. 2, which are obtained from the Fourier transform of Eqs. (9) and (10). It is observed that the harmonic spectra of the Γ (\mathbf{k}_0) channel and the boundary of the first BZ

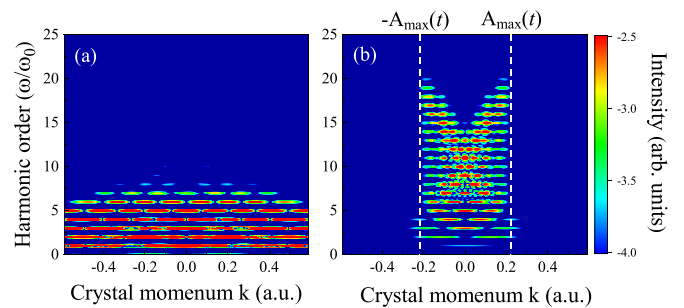


FIG. 2. (a) \mathbf{k} -resolved intraband harmonic spectrum. (b) \mathbf{k} -resolved interband harmonic spectrum. The vertical white dashed lines represent the momenta corresponding to the values of the maximum vector potential $\pm \mathbf{A}_{\max}(t) = \pm 0.22$ a.u..

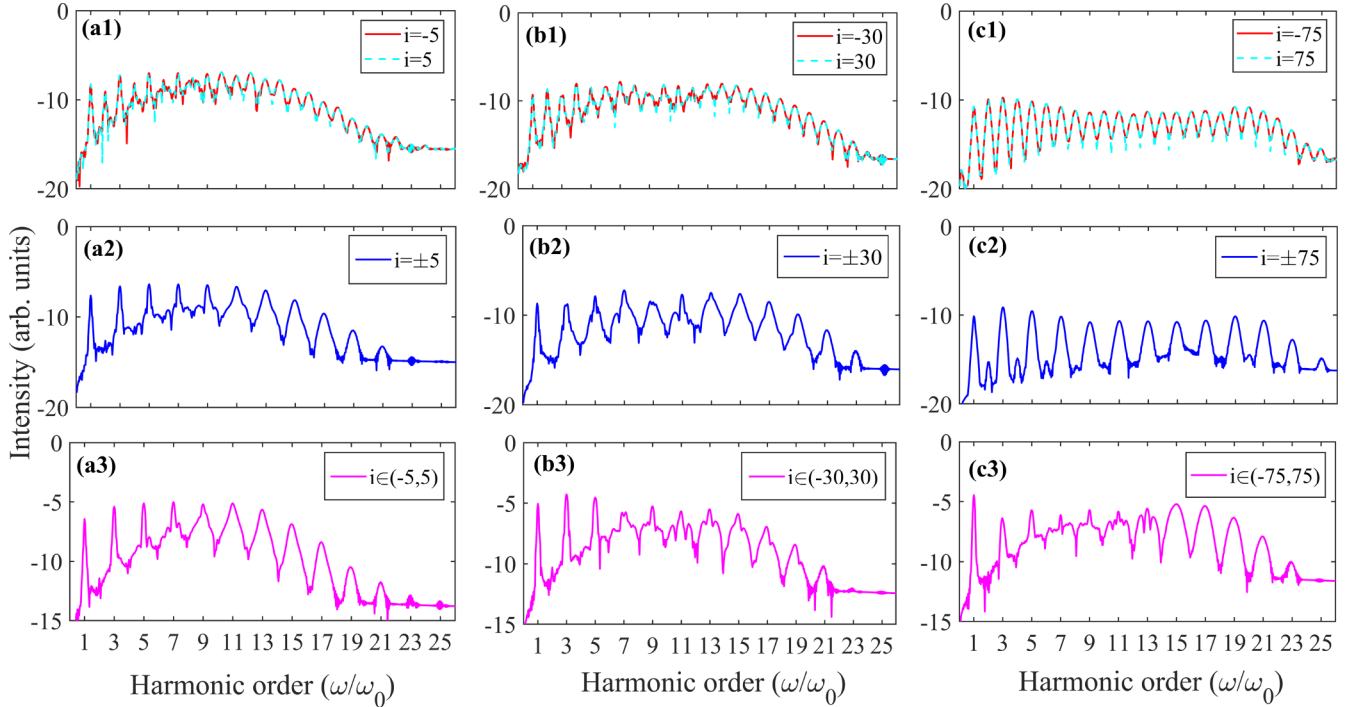


FIG. 3. (a1) Interband harmonic spectra corresponding to \mathbf{k}_{-5} (red solid line) and \mathbf{k}_5 (cyan dashed line) channels. (a2) Total interband harmonic spectrum of two symmetric channels $\mathbf{k}_{\pm 5}$. (a3) Interband harmonic spectrum generated by the sum of all channels in the extended region $i \in (-5, 5)$. (b1)–(b3) The same as (a1)–(a3) but for \mathbf{k}_{-30} , \mathbf{k}_{30} , $\mathbf{k}_{\pm 30}$, and $i \in (-30, 30)$. (c1)–(c3) The same as (a1)–(a3) but for \mathbf{k}_{-75} , \mathbf{k}_{75} , $\mathbf{k}_{\pm 75}$, and $i \in (-75, 75)$.

($\mathbf{k}_{\pm 200}$) exclusively consist of odd-order harmonics. Besides, both even- and odd-order harmonics will be exhibited for each \mathbf{k}_i channel [35,38]. In Fig. 2(b), the interband harmonic radiation is limited by the maximum laser vector potential $\pm \mathbf{A}_{\max}(t)$ [indicated by the two vertical white dashed lines]. The V-shaped cutoff position of interband HHG for each \mathbf{k}_i channel is limited by the band gap [38].

By comparing Figs. 2(a) and 2(b), one can see that the intraband harmonics dominate the HHG at harmonic photon energies below the band gap ($\varepsilon_g \approx 6\omega_0$). This observation demonstrates that the harmonic subpeak structures in Fig. 1(a), ranging from the 7th to the 13th order, are primarily from the interband harmonics. In Fig. 2(b), it is notable that the crystal momenta around the \mathbf{k}_0 channel significantly contribute to the 7th–13th order harmonics. However, for harmonics above the 13th order, the crystal momenta around the \mathbf{k}_0 channels have little contribution to the interband HHG. The corresponding spectrum of harmonics above the 13th order in Fig. 1(a) only exhibits odd-order harmonics without subpeak structure. Thus, the subpeak structures may originate from the interband harmonics generated by the crystal momenta around the \mathbf{k}_0 channel.

Figure 3(a1) shows the harmonic spectrum generated by the individual channel \mathbf{k}_{-5} (\mathbf{k}_5). We can see that the harmonic spectrum exhibits both even- and odd-order harmonics. Figure 3(a2) shows the harmonic spectrum generated by two symmetric channels $\mathbf{k}_{\pm 5}$. The harmonic spectrum is dominated by odd-order harmonics. Thus, the interferences between harmonics generated by different \mathbf{k} channels play a key role in spectral structures, as previously demonstrated in Ref. [35]. In Fig. 3(a3), we show the harmonic generated

by the sum of all crystal momentum channels \mathbf{k}_i in the extended region $i \in (-5, 5)$, i.e., replacing the integral in Eq. (4) $\int_{BZ} d\mathbf{K} \rightarrow \int_{(\mathbf{k}_{-5}, \mathbf{k}_5)} d\mathbf{K}$ [39]. We can see only odd-order harmonics without subpeak structure in the harmonic spectrum.

Figures 3(b1) and 3(c1) show the harmonic spectra generated by individual channels \mathbf{k}_{-30} (\mathbf{k}_{30}) and \mathbf{k}_{-75} (\mathbf{k}_{75}), respectively. The harmonic spectra exhibit both even- and odd-order harmonics, which is similar to the case as shown in Fig. 3(a1). Figures 3(b2) and 3(c2) display the harmonic spectra generated by two symmetric channels $\mathbf{k}_{\pm 30}$ and $\mathbf{k}_{\pm 75}$, respectively. The harmonic spectra only exhibit odd-order harmonics, which is similar to the case as shown in Fig. 3(a2). Figures 3(b3) and 3(c3) present the harmonic spectra generated by the sum of all crystal momentum channels \mathbf{k}_i in the extended regions $i \in (-30, 30)$ and $i \in (-75, 75)$. We can see that as the number of selected channels increases, the subpeak structures of the 7th to 13th harmonic appear. Referring back to Fig. 2(b), it is established that harmonic radiation is bounded by the maximum vector potential $\pm \mathbf{A}_{\max}(t)$, which corresponds to the region $i \in (-75, 75)$. Thus, the harmonic spectrum presented in Fig. 3(c3) coincides with the harmonic spectrum generated by all \mathbf{k}_i channels in the first BZ, as demonstrated in Fig. 1(a).

The q th harmonic intensity is determined by the coherent superposition of two harmonic fields $S_q^{\mathbf{k}_1}$ and $S_q^{\mathbf{k}_2}$, generated by crystal momentum channels \mathbf{k}_1 and \mathbf{k}_2 . Thus, the q th harmonic intensity can be written as [35]

$$\begin{aligned}
 S_q &= |S_q^{\mathbf{k}_1} + S_q^{\mathbf{k}_2}|^2 \\
 &= |S_q^{\mathbf{k}_1}|^2 + |S_q^{\mathbf{k}_2}|^2 + 2\sqrt{|S_q^{\mathbf{k}_1}|^2 |S_q^{\mathbf{k}_2}|^2} \cos \Delta\varphi_q, \quad (11)
 \end{aligned}$$

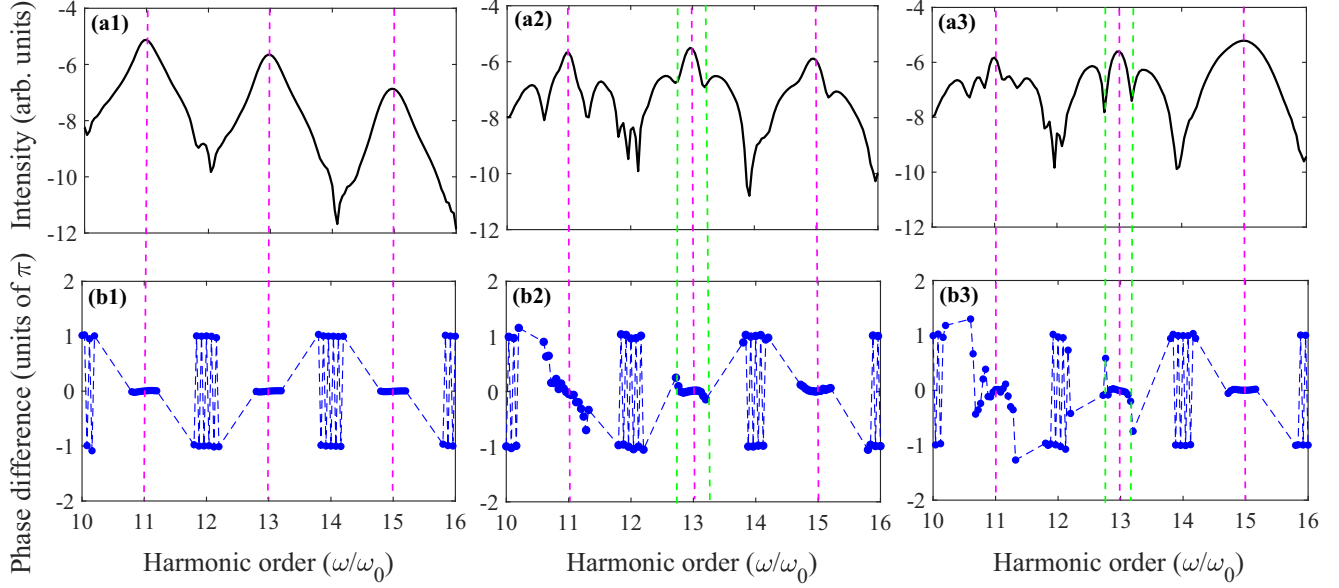


FIG. 4. (a1)–(a3) The interband harmonic spectra of 10th–16th order generated by the sum of all channels \mathbf{k}_i in the extended regions $i \in (-5, 5)$, $i \in (-30, 30)$ and $i \in (-75, 75)$, respectively. (b1)–(b3) The corresponding harmonic phase difference of symmetric crystal momentum channels.

where $\Delta\varphi_q = \varphi_q^{\mathbf{k}_1} - \varphi_q^{\mathbf{k}_2}$ is the phase difference of harmonic fields $S_q^{\mathbf{k}_1}$ and $S_q^{\mathbf{k}_2}$. For the case of harmonic spectrum generated by the sum of all crystal momentum channels \mathbf{k}_i in the extended region $i \in (-m, m)$, we can rewrite Eq. (11) in the form

$$\begin{aligned} S'_q &= |S_q^{\mathbf{k}_{(-m,0)}} + S_q^{\mathbf{k}_{(0,m)}}|^2 \\ &= |S_q^{\mathbf{k}_{(-m,0)}}|^2 + |S_q^{\mathbf{k}_{(0,m)}}|^2 + 2\sqrt{|S_q^{\mathbf{k}_{(-m,0)}}|^2 |S_q^{\mathbf{k}_{(0,m)}}|^2} \cos\Delta\varphi'_q, \end{aligned} \quad (12)$$

where $|S_q^{\mathbf{k}_{(-m,0)}}|^2$ represents the harmonic calculated by the sum of the currents from the \mathbf{k}_{-m-1} channel to the \mathbf{k}_{-1} channel and $|S_q^{\mathbf{k}_{(0,m)}}|^2$ represents the harmonic calculated by the sum of the currents from the \mathbf{k}_1 channel to the \mathbf{k}_{m-1} channel. $2\sqrt{|S_q^{\mathbf{k}_{(-m,0)}}|^2 |S_q^{\mathbf{k}_{(0,m)}}|^2} \cos(\Delta\varphi'_q)$ represents the interference term of harmonics generated by a set of symmetric crystal momentum channels. $\Delta\varphi'_q = \varphi_{\mathbf{k}_{(-m,0)}} - \varphi_{\mathbf{k}_{(0,m)}}$ is the phase difference of the harmonic fields $S_q^{\mathbf{k}_{(-m,0)}}$ and $S_q^{\mathbf{k}_{(0,m)}}$.

To illustrate the original subpeak structures of the harmonics, Figs. 4(a1)–4(a3) show the partial enlargement of Figs. 3(a3)–3(c3), i.e., the harmonic spectra from 10th to 16th order. Figures 4(b1)–4(b3) show the corresponding harmonic phase differences. For the harmonic spectrum generated by the sum of all crystal momentum channels \mathbf{k}_i in the extended region $i \in (-5, 5)$ [see Figs. 4(a1) and 4(b1)], we can see that the harmonic phase difference $\Delta\varphi' = \varphi_{\mathbf{k}_{(-5,0)}} - \varphi_{\mathbf{k}_{(0,5)}} = 0$ for the odd-order harmonics, and then the $\cos\Delta\varphi' = 1$. Thus, the odd-order harmonics generated by the sum of all crystal momentum channels \mathbf{k}_i in the extended region $i \in (-5, 5)$ are constructive interferences (magenta dashed lines), while the harmonic phase difference $\Delta\varphi' = \pm\pi$ for the even-order harmonics, and then the $\cos\Delta\varphi' = -1$. Consequently, the

even-order harmonics generated by the sum of all crystal momentum channels \mathbf{k}_i in the extended region $i \in (-5, 5)$ are destructive interferences [35]. This explains the prevalence of odd-order harmonics in the harmonic spectrum, as demonstrated in Figure 4(a1). The harmonic spectra dominated by the odd-order harmonics can also be observed in the crystal momentum channels \mathbf{k}_i with $i \in (-30, 30)$ and $i \in (-75, 75)$, as shown in Figs. 4(a2) and 4(a3), respectively.

To demonstrate the physical mechanism of the harmonic subpeak structures, we take the vicinity of the 13th harmonic as an example in Figs. 4(b2) and 4(b3). As the number of crystal momentum channels \mathbf{k}_i increases, the harmonic phase differences corresponding to the positions of subpeak structures are closer to $\pm\pi$ (green dashed lines). Thus, the destructive interference occurs gradually, which results in the subpeak structures in the harmonic spectra. Our results demonstrated that the subpeak structures originate from the interferences between the interband harmonics, which are generated by different crystal momenta channels around the top of the V-B. The similar subpeak structures in Ref. [34] have been interpreted as a result of the quantum path interference. Clearly, the subpeak structures in Ref. [34] and our work have different origins.

B. Suppression of harmonic subpeak structures by the two-color laser field

Figure 5(a) displays the HHG spectra driven by the two-color $(\omega_0, 3\omega_0)$ laser pulse with field ratio $E_1/E_0 = 0.4$ and the relative phase $\phi = \pi$. Additionally, we also investigated the harmonic spectra driven by the two-color laser fields with different frequencies of the second component $[(\omega_0, 2\omega_0); (\omega_0, 4\omega_0); (\omega_0, 5\omega_0), \text{etc.}]$. In the case of two-color laser fields $(\omega_0, 2\omega_0)$ and $(\omega_0, 4\omega_0)$, the harmonic

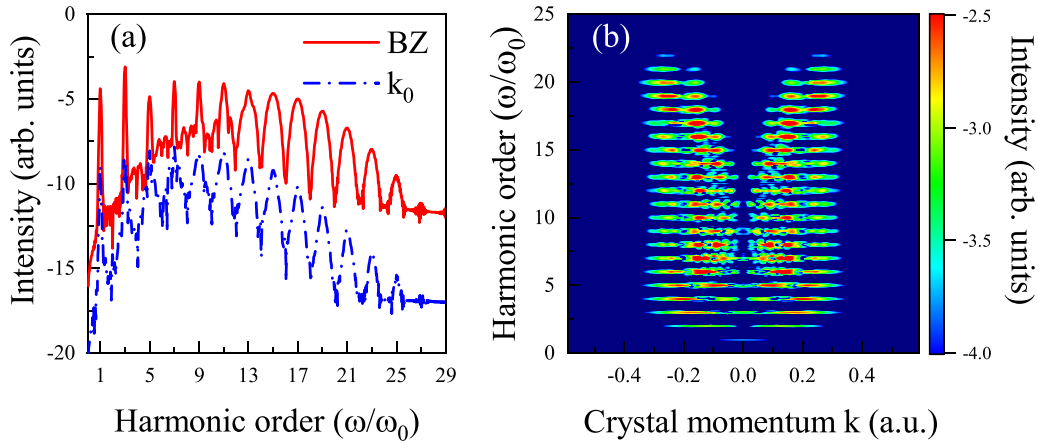


FIG. 5. (a) The interband harmonic spectra integrated over the first BZ (red solid line) and generated by the \mathbf{k}_0 channel (blue dotted-dashed line) driven by the two-color laser field. (b) The corresponding \mathbf{k} -resolved interband harmonic spectrum. The other laser parameters are the same as those in Fig. 1(a).

spectra exhibit both odd- and even-order harmonics without subpeak structure [14]. In this work, we primarily focus on analyzing the fine structures of the harmonic spectra. To maintain consistency with the harmonic spectrum displaying exclusively odd-order harmonics driven by the one-color laser field, we did not select the second component to be the two and four harmonic fields. For the two-color laser field ($\omega_0, 5\omega_0$) case, the harmonic spectrum consists of odd-order harmonics without subpeak structure, which is similar to the two-color laser field ($\omega_0, 3\omega_0$) case. Therefore, we choose the third harmonic as the second component. Furthermore, we find that the subpeak structures are insensitive to the amplitude of the second component but sensitive to the relative phase. When the relative phase is chosen to be $\phi = \pi$, the subpeak structures are completely suppressed. We set the field ratio $E_1/E_0 = 0.4$ such that the maximum amplitude of the two-color laser field is about the same as that of the one-color laser field.

Figure 5(a) clearly demonstrates the effective suppression of subpeak structures in the harmonic spectrum when integrated over the first BZ (red solid line). Comparing this result with the one-color laser field case, we observe a significant enhancement in the harmonic intensities, by approximately one to two orders of magnitude. This enhancement aligns with findings from previous studies [17–19], where it was shown that the peak intensities of two-color laser fields can surpass the maximum amplitudes of one-color laser pulses. Since the HHG in solids depends crucially on the peak intensity of the driving field, the harmonic yields were obviously enhanced. However, it is important to note that in this study, we have managed to make the two-color field have the same peak electric field as the one-color laser field. It is expected that a different mechanism of harmonic radiation is responsible for the enhancement of harmonics. We also investigate the harmonic spectrum considering only the \mathbf{k}_0 channel (blue dotted-dashed line) driven by the two-color laser field, which exhibits odd-order harmonics without subpeak structure. Additionally, it is noticed that the harmonic intensity generated by the \mathbf{k}_0 channel is four to five orders of magnitude

lower than that of the harmonic spectrum integrated over the first BZ.

In Fig. 5(b), we illustrate the \mathbf{k} -resolved interband harmonic spectrum in the two-color laser field. When compared to the case of a one-color laser field, the crystal momentum channels which contribute to the harmonic radiation are extended. Besides, one can see that the crystal momenta around the \mathbf{k}_0 channel make little contribution to the interband harmonics, which is similar to the case of the harmonics above the 13th order in the one-color laser field [see Fig. 2(b)]. The contribution decrease from the crystal momenta around the \mathbf{k}_0 channel results in the suppression of the harmonic subpeak structures.

Figure 6(a1) illustrates the electric field and the corresponding vector potential for the one-color laser pulse. When the electric field reaches its maximum peak (magenta dashed line), the corresponding vector potential is equal to zero. In Figs. 6(a2) and 6(a3), we show the time-dependent C-B population in the initial momentum frame and in the moving crystal momentum frame, respectively. We can see that the C-B population increases rapidly around the \mathbf{k}_0 channel when the electric field reaches its maximum value (the corresponding vector potential is equal to 0). The same situation that the C-B population increases rapidly around $\mathbf{K} = 0$ can be seen in the moving frame as shown in Fig. 6(a3). Thus, the electrons are excited to C-B around the \mathbf{k}_0 channel by the laser field, which results in the crystal momenta around the \mathbf{k}_0 channel having a significant contribution to the HHG for the one-color laser field [see Fig. 2(b)].

Figure 6(b1) presents the electric field and the corresponding vector potential for the two-color laser pulse. When the electric field reaches its maximum peaks, the corresponding vector potentials are equal to ± 0.15 a.u.. Figure 6(b2) provides the corresponding time-dependent population of C-B in the initial crystal momentum frame. It should be noticed that the population has two excitation bursts around $\mathbf{k} = \pm 0.15$ a.u. channels (see the two horizontal white dashed lines). However, the C-B population increases also around $\mathbf{K} = 0$ in the moving crystal momentum frame as shown in Fig. 6(b3).

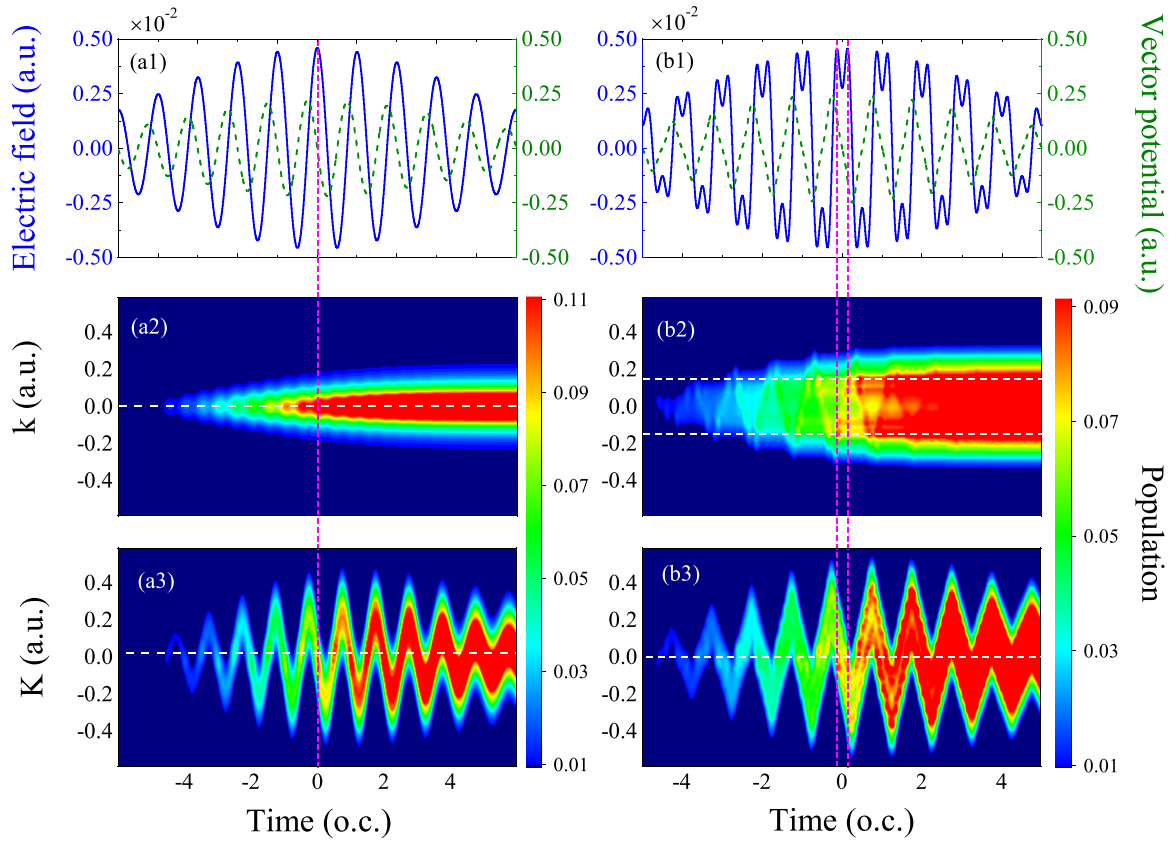


FIG. 6. (a1 and b1) The electric field (blue solid line) and vector potential (green dashed line) for the one-color and the two-color laser fields. (a2 and b2) The corresponding time-dependent C-B population in the initial crystal momentum frame \mathbf{k} . (a3 and b3) The corresponding time-dependent C-B population in the moving frame \mathbf{K} . The vertical magenta dashed lines represent the temporal positions of the maximum amplitudes of the electric fields.

This behavior aligns with the four-step model of solid HHG [11,12], i.e., the electrons around $\mathbf{k} = \pm 0.15$ a.u. channels are preaccelerated to the top of the V-B before being excited to the C-B, as previously demonstrated in Ref. [12]. The intraband preacceleration of electrons could influence the interband excitation and enhance the intensity of the HHG. Consequently, the crystal momenta around the \mathbf{k}_0 channel make little contribution to the HHG for the two-color laser field [see Fig. 5(b)] due to the decrease of contribution from the crystal momenta around the \mathbf{k}_0 channel, akin to the harmonics above the 13th order in the one-color laser field, suppressing the harmonic subpeak structures.

IV. CONCLUSIONS

In summary, our study delved into the phenomenon of solid HHG driven by both one-color and two-color linearly polarized laser pulses. We observed subpeak structures in the harmonic spectrum when employing a one-color laser field. To illustrate the underlying mechanism behind these fine structures, we analyzed the crystal-momentum-resolved contributions of the intra- and interband harmonics. The results show that the harmonic subpeaks are due to the interferences between the interband harmonics generated by the crystal momenta around the \mathbf{k}_0 channel. By analyzing harmonic phase differences, we provided a detailed demonstration of constructive and destructive interferences within the HHG process.

Furthermore, we explored the harmonic spectrum generated by a two-color laser field and observed the effective suppression of fine structures. Our analysis revealed that the crystal momenta around the \mathbf{k}_0 channel make little contributions to HHG, which is related to the preacceleration process of electrons. In this work, we have focused on the two-band insulator model based on ZnO. The inclusion of multibands will lead to important contributions to solid HHG [39,42–44], such as multiple plateaus [39] and even-order harmonic generation [43]. Based on the multiband SBEs, a microscopic method has been proposed to investigate high harmonic generation in solids with band crossings [44]. Further investigations could delve into the impact of the multiband scenario and band crossings on the solid HHG. We expect our work to be helpful in gaining insight into the ultrafast electron-hole dynamics in solid HHG.

ACKNOWLEDGMENTS

We thank Xi Zhao for his critical reading of the manuscript. This work was supported by the Natural Science Foundation of Jilin Province of China (Grant No. 20230101014JC), the National Natural Science Foundation of China (Grant No. 12374265), and the Scientific and Technological Research Project of the Education Department of Jilin Province, China (Grant No. JJKH20231125KJ).

- [1] A. L'Huillier and P. Balcou, *Phys. Rev. Lett.* **70**, 774 (1993).
- [2] Z. Chang, A. Rundquist, H. Wang, M. M. Murnane, and H. C. Kapteyn, *Phys. Rev. Lett.* **79**, 2967 (1997).
- [3] R. Kienberger, M. Hentschel, M. Uiberacker, C. Spielmann, M. Kitzler, A. Scrinzi, M. Wieland, T. Westerwalbesloh, U. Kleineberg, U. Heinzmann, M. Drescher, and F. Krausz, *Science* **297**, 1144 (2002).
- [4] J. Zhang, X.-L. Ge, T. Wang, T.-T. Xu, J. Guo, and X.-S. Liu, *Phys. Rev. A* **92**, 013418 (2015).
- [5] H. Yang, P. Liu, R. Li, and Z. Xu, *Opt. Express* **21**, 28676 (2013).
- [6] X.-X. Huo, S. Wang, L. Sun, Y.-H. Xing, J. Zhang, and X.-S. Liu, *Phys. Rev. A* **106**, 023102 (2022).
- [7] P. B. Corkum, *Phys. Rev. Lett.* **71**, 1994 (1993).
- [8] S. Ghimire, A. D. DiChiara, E. Sistrunk, P. Agostini, L. F. DiMauro, and D. A. Reis, *Nat. Phys.* **7**, 138 (2011).
- [9] Y. S. You, D. A. Reis, and S. Ghimire, *Nat. Phys.* **13**, 345 (2017).
- [10] G. Ndabashimiye, S. Ghimire, M. Wu, D. A. Browne, K. J. Schafer, M. B. Gaarde, and D. A. Reis, *Nature (London)* **534**, 520 (2016).
- [11] L. Li, P. Lan, X. Zhu, T. Huang, Q. Zhang, M. Lein, and P. Lu, *Phys. Rev. Lett.* **122**, 193901 (2019).
- [12] X. Song, S. Yang, R. Zuo, T. Meier, and W. Yang, *Phys. Rev. A* **101**, 033410 (2020).
- [13] Y.-L. He, J. Guo, F.-Y. Gao, and X.-S. Liu, *Phys. Rev. B* **105**, 024305 (2022).
- [14] Y. Wang, T. Shao, X. Li, Y. Liu, P. Jiang, W. Zheng, L. Zhang, X.-B. Bian, Y. Liu, Q. Gong, and C. Wu, *Opt. Express* **31**, 3379 (2023).
- [15] G. Vampa, C. R. McDonald, G. Orlando, D. D. Klug, P. B. Corkum, and T. Brabec, *Phys. Rev. Lett.* **113**, 073901 (2014).
- [16] J.-B. Li, X. Zhang, S.-J. Yue, H.-M. Wu, B.-T. Hu, and H.-C. Du, *Opt. Express* **25**, 18603 (2017).
- [17] B. D. Bruner, A. J. Narovlansky-Uzan, T. Arusi-Parpar, G. Orenstein, A. Shonfeld, and N. Dudovich, *J. Phys. B: At. Mol. Opt. Phys.* **54**, 154001 (2021).
- [18] F. Navarrete and U. Thumm, *Phys. Rev. A* **102**, 063123 (2020).
- [19] X.-S. Kong, H. Liang, X.-Y. Wu, L. Geng, W.-D. Yu, and L.-Y. Peng, *J. Chem. Phys.* **156**, 074701 (2022).
- [20] C.-M. Wang, T.-S. Ho, and S.-I. Chu, *J. Phys. B: At. Mol. Opt. Phys.* **49**, 225401 (2016).
- [21] L. Li, P. Lan, L. He, W. Cao, Q. Zhang, and P. Lu, *Phys. Rev. Lett.* **124**, 157403 (2020).
- [22] M. Borsch, C. P. Schmid, L. Weigl, S. Schlauderer, N. Hofmann, C. Lange, J. T. Steiner, S. W. Koch, R. Huber, and M. Kira, *Science* **370**, 1204 (2020).
- [23] H. Liu, Y. Li, Y. S. You, S. Ghimire, T. F. Heinz, and D. A. Reis, *Nat. Phys.* **13**, 262 (2017).
- [24] T. T. Luu and H. J. Wörner, *Nat. Commun.* **9**, 916 (2018).
- [25] F. Langer, M. Hohenleutner, C. P. Schmid, C. Poellmann, P. Nagler, T. Korn, C. Schüller, M. S. Sherwin, U. Huttner, J. T. Steiner, S. W. Koch, M. Kira, and R. Huber, *Nature (London)* **533**, 225 (2016).
- [26] S. Jiang, C. Yu, G. Yuan, T. Wu, Z. Wang, and R. Lu, *J. Phys.: Condens. Matter* **29**, 275702 (2017).
- [27] Y. Lang, Z. Peng, J. Liu, Z. Zhao, and S. Ghimire, *Phys. Rev. Lett.* **129**, 167402 (2022).
- [28] A. J. Uzan-Narovlansky, Á. Jiménez-Galán, G. Orenstein, R. E. F. Silva, T. Arusi-Parpar, S. Shames, B. D. Bruner, B. Yan, O. Smirnova, M. Ivanov, and N. Dudovich, *Nat. Photon.* **16**, 428 (2022).
- [29] T. Kanai, S. Minemoto, and H. Sakai, *Nature (London)* **435**, 470 (2005).
- [30] X. Zhou, R. Lock, W. Li, N. Wagner, M. M. Murnane, and H. C. Kapteyn, *Phys. Rev. Lett.* **100**, 073902 (2008).
- [31] C. M. Heyl, J. Gädde, U. Höfer, and A. L'Huillier, *Phys. Rev. Lett.* **107**, 033903 (2011).
- [32] L.-L. Du, G.-L. Wang, P.-C. Li, X.-X. Zhou, and Z.-X. Zhao, *Phys. Rev. A* **97**, 023404 (2018).
- [33] X.-Q. Wang, Y. Xu, X.-H. Huang, and X.-B. Bian, *Phys. Rev. A* **98**, 023427 (2018).
- [34] Y. W. Kim, T.-J. Shao, H. Kim, S. Han, S. Kim, M. Ciappina, X.-B. Bian, and S.-W. Kim, *ACS Photonics* **6**, 851 (2019).
- [35] Y.-L. He, J. Guo, F.-Y. Gao, Z.-J. Yang, S.-Q. Zhang, and X.-S. Liu, *Phys. Rev. A* **104**, 013104 (2021).
- [36] V. Szaszkó-Bogár, P. Földi, I. Magashegyi, and K. Varjú, *Appl. Sci.* **9**, 1572 (2019).
- [37] L.-J. Lü and X.-B. Bian, *Phys. Rev. B* **100**, 214312 (2019).
- [38] F. Navarrete, M. F. Ciappina, and U. Thumm, *Phys. Rev. A* **100**, 033405 (2019).
- [39] C. Yu, H. Iravani, and L. B. Madsen, *Phys. Rev. A* **102**, 033105 (2020).
- [40] G. Vampa, C. R. McDonald, G. Orlando, P. B. Corkum, and T. Brabec, *Phys. Rev. B* **91**, 064302 (2015).
- [41] F. Bloch, *Z. Phys.* **52**, 555 (1929).
- [42] P. G. Hawkins, M. Y. Ivanov, and V. S. Yakovlev, *Phys. Rev. A* **91**, 013405 (2015).
- [43] G.-R. Jia, X.-H. Huang, and X.-B. Bian, *Opt. Express* **25**, 23654 (2017).
- [44] L. H. Thong, C. Ngo, H. T. Duc, X. Song, and T. Meier, *Phys. Rev. B* **103**, 085201 (2021).